Few-Layer Graphene Shells and Nonmagnetic Encapsulates: A Versatile and Nontoxic Carbon Nanomaterial

Alicja Bachmatiuk,[†,‡,§] Rafael G. Mendes,[†] Cordula Hirsch,[⊥] Carsten Jähne,[∥] Martin R. Lohe,[#] Julia Grothe,[#] Stefan Kaskel,[#] Lei Fu,[△] Rüdiger Klingeler,[∥] Jürgen Eckert,[†] Peter Wick,[⊥] and Mark H. Rümmeli[‡,§,*]

[†]IFW Dresden, P.O. Box 270116, 01069 Dresden, Germany, [‡]IBS Center for Integrated Nanostructure Physics, Institute for Basic Science (IBS), Daejon 305-701, Republic of Korea, [§]Department of Energy Science and Department of Physics, Sungkyunkwan University, Suwon 440-746, Republic of Korea, [⊥]Empa, Swiss Federal Laboratories for Materials Science and Technology, St. Gallen, Switzerland, [∥]Kirchhoff Institute for Physics, University of Heidelberg, INF 227, D-69221 Heidelberg, Germany, [#]Technische Universität Dresden, D-01062 Dresden, Germany, and [△]College of Chemistry and Molecular Science, Wuhan University, 430072 Wuhan, China

ABSTRACT In this work a simple and scalable approach to coat nonmagnetic nanoparticles with few-layer graphene is presented. In addition, the easy processing of such nanoparticles to remove their core, leaving only the 3D graphene nanoshell, is demonstrated. The samples are comprehensively characterized, as are their versatility in terms of functionalization and as a material for electrochemical storage. Indeed, these 3D graphene nanostructures are easily functionalized much as is found with carbon nanotubes and planar graphene. Electrochemical investigations indicate these nanostructures are promising for stable long-life battery applications. Finally, initial toxicological investigations suggest no acute health risk from these 3D graphene nanostructures.

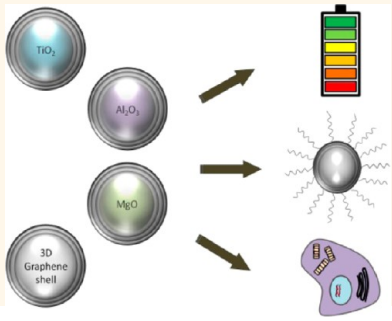

KEYWORDS: graphene nanostructures · graphene-coated oxide nanoparticles · cyclic voltammetry studies · toxicity tests

A single layer of carbon atoms with sp^2 hybridization arranged in a honeycomb lattice known as graphene shows exceptional structural,[1] physical,[2] and chemical properties[3] and has captured the imagination and attention of many research groups. Graphene and its few-layer counterparts show amazing potential in numerous applications and is driving cutting edge research in areas related to energy storage,[4] electronic devices,[5] biomedical applications,[6] and material science.[7]

When mechanically isolated graphene from highly ordered pyrolitic graphite was first reported,[8] the research world turned to finding new and cheap methods to obtain graphene with comparable structural quality, *viz.*, a near perfect carbon atom arrangement in a honeycomb lattice with analogous properties. This has led to an explosion in routes for synthetic graphene. The primary routes include the chemical exfoliation of graphite,[9] thermal sublimation of epitaxial silicon carbide,[10] and chemical vapor deposition (CVD) of hydrocarbons (over single crystals,[11] metal foils,[12] thin films,[13] and nanoparticles[14]). Of these fabrication routes, CVD shows the most promise due to its easy scale-up potential and ease of use and that it is already a well-established technique in many industrial applications. Moreover, fabrication of graphene can be accomplished over nanoparticles, making it a simple and attractive means for the preparation of three-dimensional (3D) nanostructured graphene.[15] 3D nanostructured graphene holds promise in applications such as sensors,[16] supercapacitors,[17] and catalytic electrodes.[18] In addition, 3D graphene nanostructures, like other sp^2 carbon nanomaterials, are easily surface functionalized. They may also be filled (in their core). In other words, they can carry payloads, for example, with magnetic metals or drugs for biomedical applications. Thus, 3D graphene nanostructures show potential in a variety of applications.

The easiest way to form 3D graphene nanostructures is by their synthesis over specific nanoparticles, *viz.*, templated growth. There are three main types of the nanoparticles that can be used as templates, namely, metals,[15] oxides,[19−21] and carbides.[22] Metal- and oxide-based structures have a big advantage over carbide-based structures in that they

* Address correspondence to mhr1967@yahoo.com.

Received for review May 21, 2013 and accepted November 7, 2013.

Published online November 07, 2013
10.1021/nn4051562

can easily be removed from the core using straightforward wet chemical approaches (*e.g.* dissolving in acids), whereas carbides are highly challenging to eliminate. The use of metal nanoparticles, for example, nickel, provides a relatively cheap way to fabricate graphene-coated core shell nanostructures through a carburization process. In general, the metal cores are also easily eliminated through post-synthesis treatment *e.g.*, hydrochloric acid removal.[15] However, in the case of metal nanoparticle removal there is always the risk of metal remnants after the purification process, making the 3D graphene nanostructures potentially toxic. In this regard, oxide nanoparticles serving as the template surface are more attractive than metallic nanoparticles for the preparation of 3D graphene since for the most part they are far less toxic. Moreover, their morphology means they are not susceptible to pathogenic effects in the mesothelium due to frustrated phagocytosis as are 1D fibers (*e.g.*, carbon nanotubes, asbestos).[23,24]

Here we present a cheap and scalable fabrication route for three-dimensional nanostructured graphene over oxide nanopowders *via* a simple ethanol feedstock thermal CVD approach. We thoroughly characterize the as-produced and processed synthetic materials as well as examine their potential for further functionalization and electrochemical application and test their toxicity. To process the material, we remove the core by simple dissolution in diluted acid to yield pure 3D hollow graphene nanostructures.

RESULTS AND DISCUSSION

Application of the CVD route in which the oxide nanopowders (Al_2O_3, TiO_2, or MgO) are exposed to ethanol vapor at a temperature of 775 °C for a nominal time leads to the initially white powder turning black (see Figure S1 in the Supporting Information). Detailed TEM investigations show a layered material on the surface of the nanoparticles with an interlayer spacing between 0.3 and 0.4 nm, which is typical for few-layer graphene coatings (see Figure 1).

Systematic TEM evaluations enable one to extract some statistics on the mean particle size and range as well as the average number of graphene layers. These are provided in Table 1 for the three oxides explored (Al_2O_3, TiO_2, or MgO).

In addition, a fourth sample was prepared in which as produced material using MgO nanopowder was then subjected to diluted HCl to dissolve away the core MgO and leave a graphitic shell (see panel d in Figure 1, and Table 1). The shape of the shells varies, with some being round and others cubed, as can be seen in Figure S2 in the Supporting Information. This is because the shape of the inner (MgO) nanoparticle templates the graphitic coating.

EDX of all samples shows no contamination. Only carbon, traces of oxygen, and copper are present.

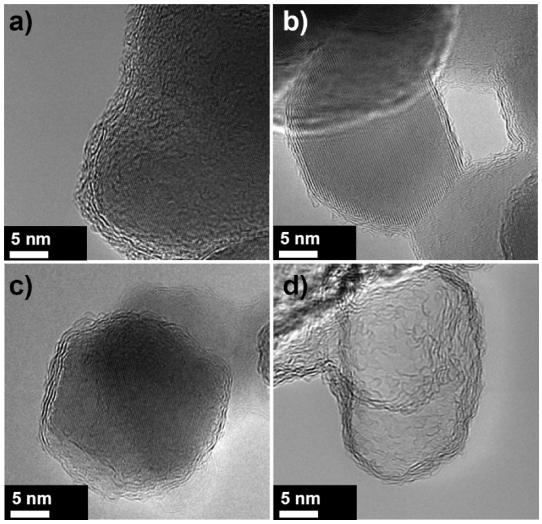

Figure 1. TEM images of graphene-coated oxide nanoparticles: (a) alumina, (b) titania, (c) magnesia, (d) carbon shells after magnesia removal.

TABLE 1. Details of the Graphene-Coated Oxide Nanoparticles and Carbon Shells Explored in the Study

	C@Al_2O_3	C@TiO_2	C@MgO	C-shells
mean diameter (nm)	110 (±1)	32 (±1)	40 (±1)	40 (±1)
size range (nm)	20–180	15–45	15–80	15–80
average C-layers	4	4	7	7
NPs (μg)	NA	2×10^{10}	9×10^{9}	4×10^{10}

The copper signal is from the TEM grid (see Figure S3 in the Supporting Information).

Raman spectroscopy is a powerful tool with which to identify the presence of sp^2 (graphitic) carbon and thus provides an ideal means to confirm the layered material that formed over the surface of the oxide nanoparticles is few-layer graphene. sp^2 carbon provides two clear signatures in Raman spectroscopy through the first-order peaks around 1350 and 1600 cm^{-1}, which are termed the D and G band, respectively. Stretching of all sp^2 carbon pairs in both rings and chains leads to the so-called G (graphitic) mode, while breathing modes of sp^2 atoms in rings lead to the D (defect) mode, since this mode is activated only by defects due to its peculiar selection rules.[25] All samples prepared in this study showed clear G and D mode signatures, as for example shown in Figure 2a. In general, the G to D mode ratios vary between 1.3 and 2, suggesting the graphitic material is rather defective. This may not necessarily be due to vacancies in the graphene layers, but to the relatively large number of edges with dangling bonds.[26] Fourier transform infrared (FTIR) spectroscopy also showed the presence of C–C stretch and hexagonal C modes between 500 and 2000 cm^{-1} (data not shown). In addition, the spectra showed weak responses corresponding to C–O and C═O stretch modes. To better investigate the samples

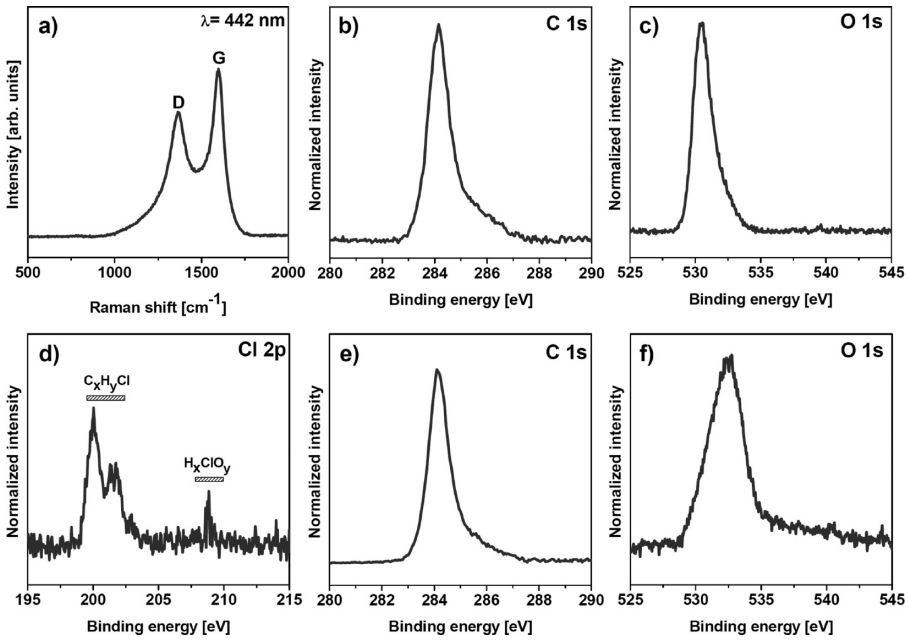

Figure 2. (Upper panel) Representative spectra of graphene-coated oxide particles: (a) Raman spectrum of G and D region, (b) XPS spectrum of C 1s region, (c) XPS spectrum of O 1s region. (Lower panel) Spectra of carbon shells after removal of MgO with dilute HCl: (d) XPS spectrum of Cl 2p region, (e) XPS spectrum of C 1s region, (f) XPS spectrum of O 1s region.

and the presence of oxygen-based species, X-ray photoelectron spectroscopy (XPS) was implemented (Figure 2, panels b through f). All as-produced samples (C@TiO_2, C@Al_2O_3, and C@MgO) exhibited C 1s edge profiles at around 284 eV, corresponding to sp^2 carbon (panel b in Figure 2). The rear tail of the C 1s edge terminates at 287 eV and so does not preclude the (weak) presence of C−O and C═O species. In the case of oxide nanoparticles coated with few-layer graphene, the O 1s edge is centered at *ca.* 531 eV, which can be attributed to O adsorbents or carbonates. However, the lack of any signal around 290 eV (carbonate signature) in the C 1s edge indicates O adsorbents dominate.

This is in agreement with the EDX data indicating only a small O fraction and the FTIR data (not shown) demonstrating any contribution from C−O and C═O species is small. In the case of the hollow shell samples, which were produced by treatment in HCl to dissolve out the MgO core, the XPS spectrum deviates from that of the as-produced samples in that the O 1s peak is weaker relative to the C 1s edge. Moreover the O 1s edge centers at around 533 eV, which suggests the presence of C−O-based species despite the sample being annealed in high vacuum. This is concomitant with findings by others in which annealing in vacuum does not fully remove oxygen-based species (although surface adsorbents are removed).[27] In addition, Cl-based species were observed (due to the HCl treatment). The XPS data showed chlorine-based species at around 200 and 210 eV, which correspond to CxHyCl and HxClOy (perchlorate) species, respectively. As will be shown later, these Cl-based species might influence the reactive oxygen species' toxicity test.

One of the attractive features of carbon nanotubes and graphene is their potential to be functionalized, thus significantly expanding their already exciting application potential. For example, functionalization can aid their solubilization,[28] allow loading of further molecules (*e.g.*, drug loading),[6] serve as a catalyst support (*e.g.*, loading with catalyst nanoparticles),[29] improve biocompatibility,[30] enable doping to modify electrical properties (*e.g.* sensors),[31] or serve as a filler in a composite that covalently bonds to the composite (*e.g.*, to improve mechanical properties)[32] to name a few. All these enhanced application potentials through functionalization are also fully applicable to 3D graphene nanostructures. To prove this functionalization versatility also applies to our samples, we now show three different and subsequent functionalization steps using graphene-coated alumina nanoparticles as the test sample. In the first functionalization step, graphene-coated alumina nanoparticles are subjected to a milling procedure (see Materials and Methods) to yield −OH functional groups on the surface. Raman spectroscopy investigations show no noticeable change in the G and D modes after functionalization with hydroxyl groups, indicating no significant deterioration in the quality of the graphene layers coating the alumina nanoparticles (Figure 3a).

FTIR observations clearly show the development of a peak between 1300 and 1500 cm^{-1}, which corresponds to −OH, confirming the successful functionalization of the graphene-coated alumina shells with OH functional groups (Figure 3b). In the second functionalization step, the −OH-functionalized graphene-coated alumina nanoparticles were subjected to a reflux

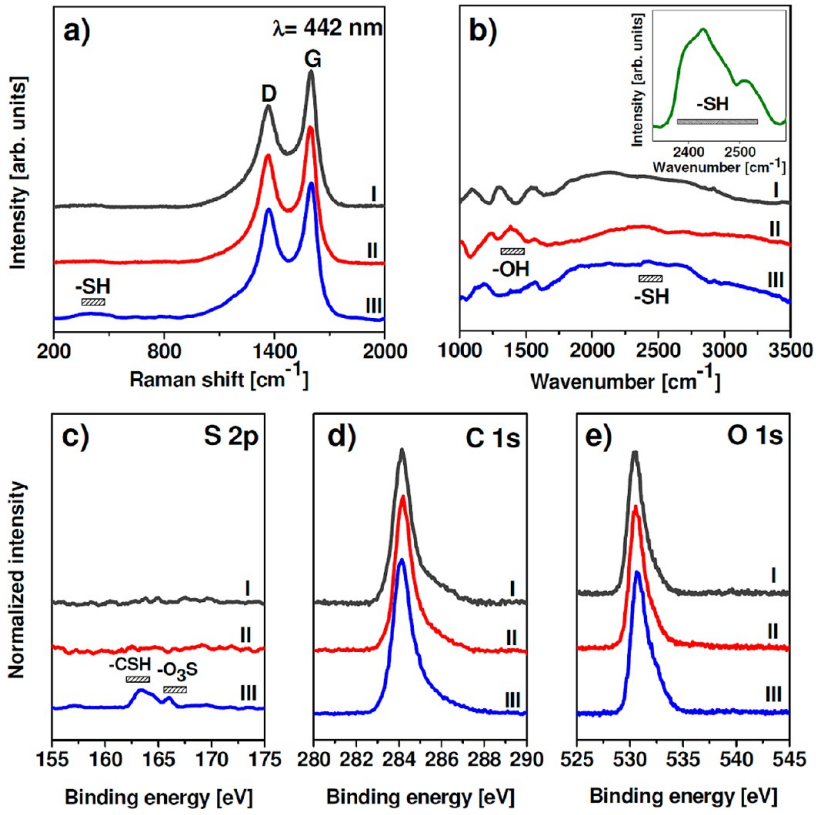

Figure 3. (a) Raman spectra, (b) infrared spectra, (c) XPS spectra of S 2p region, (d) XPS spectra of C 1s region, and (e) XPS spectra of O 1s region of graphene-coated aluminum oxide nanoparticles: (I) starting material, (II) material functionalized with hydroxide groups, (III) material functionalized with thiol groups.

treatment in P_4S_{10} and toluene to convert the hydroxyl groups to thiol (−SH) groups (see Materials and Methods). As with the first functionalization step, Raman spectroscopy investigations show no significant degradation of the sp^2 carbon. In addition, a new peak around 300 cm^{-1} indicates the presence of −SH groups. This is further confirmed by the emergence of a new peak at around 2450 cm^{-1} in the FTIR spectrum, which is attributed to −SH functional groups.[33] In the final step, the thiol-functionalized graphene-coated alumina nanoparticles are decorated with Cu nanoparticles (see Materials and Methods). The various morphological changes to the graphene-coated alumina nanoparticles over the sequential functionalization steps are shown in Figure 4, panels a through c. In panel a, the pristine sample is presented. The few-layer graphene coating is clearly visible. In panel b a nanoparticle after thiolation treatment is presented, in which a thicker amorphous coating is easily observed on the surface. In panel c a particle after the decoration treatment shows smaller nanoparticles covering a graphene-coated alumina nanoparticle. Investigations in the Fourier domain confirm the nanoparticles are copper (see for example the inset in the inset of panel c in Figure 4). X-ray diffraction (XRD) studies confirmed the presence of crystalline copper (Figure 4d). TEM measurements indicate the average size of the Cu particles varies between 5 and 15 nm.

In addition to exploring the functionalization potential of these 3D graphene nanostructures, we also looked at their potential for electrochemical storage. As our test sample here we employed the graphene-coated titania particles. This is because although the high surface area, excellent cyclability, chemical stability, and negligible toxicity in combination with a higher than carbon lithium intercalation−deintercalation potential in the range 1.5−1.7 V *vs* Li/Li+ render TiO_2 an attractive candidate for safe electrodes in lithium ion batteries, its direct application for lithium intercalation and deintercalation is limited by its poor electronic conductivity. The kinetics of the processes and hence applicability for electrochemical energy storage strongly depends on the particles' size and carbon functionalization.[34,35] Composite nanostructures such as few-layer graphene-coated titania nanoparticles provide a straightforward approach to improve electronic conductivity of uncoated TiO_2. For these reasons we chose to explore the electrochemical properties of titania nanoparticles coated with few-layer graphene for application in lithium ion batteries within a series of cyclic voltammetry (CV) and charge−discharge studies (Figure 5).

The material shows reversible cyclability, as demonstrated by the galvanostatic discharge/charge profiles of the graphene-coated anatase nanoparticles in Figure 5a

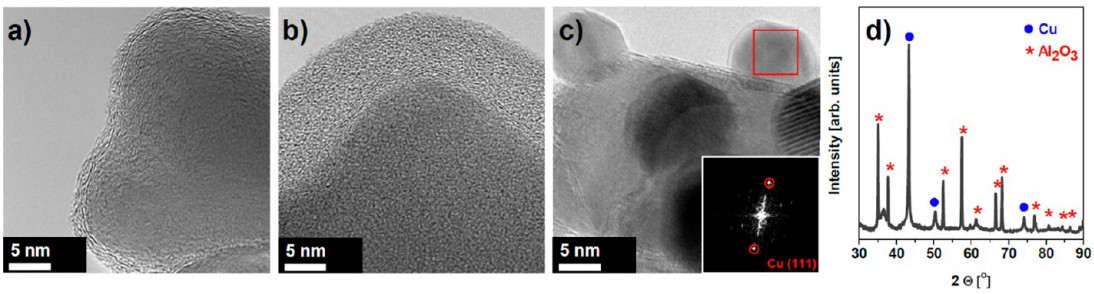

Figure 4. TEM images of graphene-coated aluminum oxide nanoparticles: (a) starting material, (b) material functionalized with thiol groups, (c) material decorated with copper particles, (d) XRD spectrum of the material decorated with copper particles.

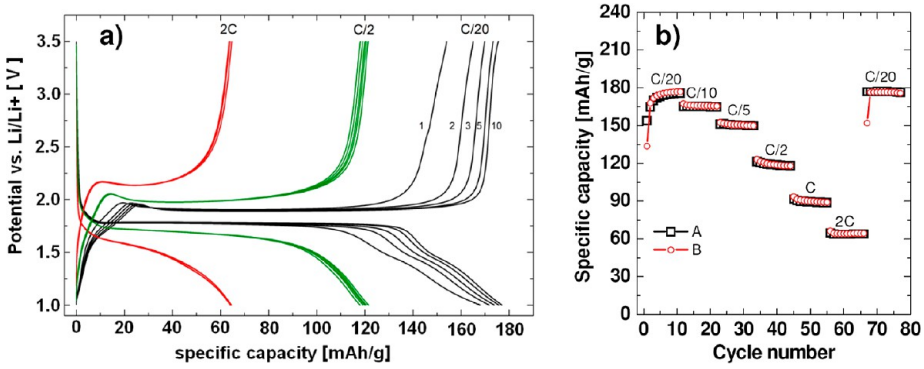

Figure 5. (a) Specific capacity for different C-rates recorded from consecutive charge−discharging cycles as follows: C/20, C/10 (not shown), C/5 (not shown), C/2, C (not shown), and 2C. For each C-rate, 10 cycles were recorded. (b) Specific capacity for consecutive charge−discharge cycling. For each C-rate 11 cycles were recorded.

and cyclic voltammetry data (provided in Figure S4 in the Supporting Information). A pronounced redox couple is found at around 2.1 V (oxidation) and 1.65 V (reduction) at similar potentials to those reported previously for bare as well as C-functionalized anatase nanoparticles.[35,36] The redox peaks are associated with lithium extraction from and insertion into the anatase structure according to the reaction

$$TiO_2 + xLi^+ + xe^- \leftrightarrow Li_xTiO_2 \quad (1)$$

A large initial overpotential for the reduction side is strongly reduced in the second cycle (see the reduction peak shift from 1.5 V to 1.65 V in Figure S4 of the Supporting Information), while the oxidative overpotential is less pronounced even in the first cycle. The overpotential is presumably associated with solid electrolyte interphase (SEI) formation, which slowly starts at around 2 V upon reduction and then accelerates below 0.9 V.[37] The formation of SEI processes similar to the exfoliation in carbon electrodes may cause cracks, thereby reducing the overpotential in subsequent cycles.[38] In particular, we assume no further SEI formation since the few graphene layers are already oxidized. This assumption is supported by the fact that the peak currents of both oxidation and reduction peaks as well as the maximum specific capacities are increasing within the first 10 cycles, while the typical behavior for anatase-based electrodes is found in the 10th to 25th cycle.

Galvanostatic discharge/charge profiles of the graphene-coated anatase nanoparticles at different C-rates provide information on the intercalation mechanism (Figure 5a). A key feature in the recorded profiles are the pronounced plateaus at about 1.78 and 1.9 V *vs* Li/Li^+ (*e.g.*, for C/20), respectively, highlighting the two-phase regime typical for anatase, and this points to the coexistence of a Li-poor $Li_{0.05}TiO_2$ phase with the anatase space group $I4_1/amd$ and a Li-rich $Li_{0.5}TiO_2$ phase exhibiting *Imma* (*e.g.*, ref 39). The width of the plateau (*cf.* ref 35) suggests that $x > 0.4$ Li ions are inserted into the interstitial octahedral sites of the bulk anatase phase Li_xTiO_2 at this voltage; that is, the overall capacity at small C-rates is dominated by this process. The data imply good cyclability for all C-rates investigated with a symmetric capacity yield for charging/discharging. Note that the initial increase of the capacity in the first couple of cycles for C/20 is due to the SEI process as discussed above. The evolution of the gravimetric capacity is summarized in Figure 5b. Disregarding initial irreversible effects, only very small capacity fades are observed for a given C-rate, which together with the recovery of the specific capacity when finally switching back to C/20 implies a high stability and excellent cyclability for this material. Moreover, the Coulombic efficiency is nearly 100% for all C-rates investigated. After 200 cycles (see Figures S5 and S6 in the Supporting Information),

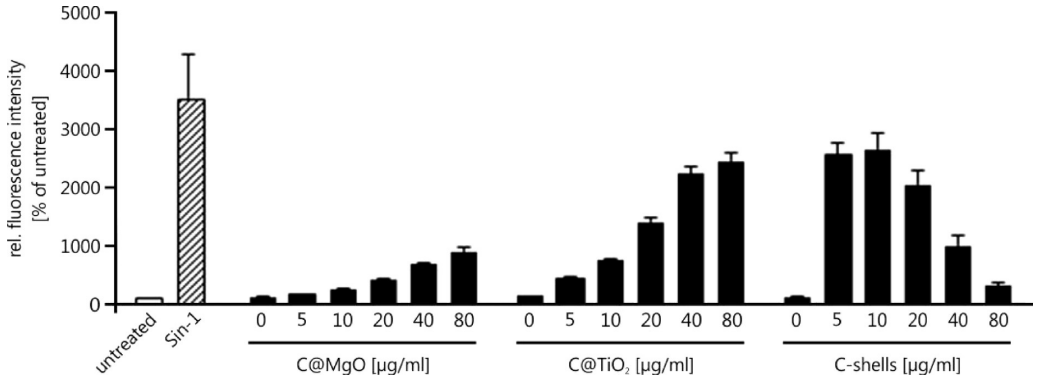

Figure 6. All three nanomaterials tested lead to elevated ROS levels. ROS formation was measured in A549 cells after two hours of treatment with indicated concentrations of C@MgO, C@TiO_2, and C-shells using the DCF assay. "0 μg/mL" constitutes the solvent controls, which correspond to 51 ppm Pluronic F-127. Sin-1 (100 μM) was used as the positive control. Original fluorescence values are blank-corrected and normalized to untreated samples. The data represent the mean of three independent experiments and the standard deviation.

the Coulombic efficiency is 99.7%, and post-mortem TEM analysis of the cycled material shows crystalline nanoparticles with fully developed C-shells coating the core particles. Namely, the material graphene-coated nanoparticles are not damaged by charging/discharging cycles.

In addition to exploring the application potential of 3D graphene nanostructures, as with all aspects of nanotechnology, it is important to also understand their impact on humans and the environment. To this end, we investigated the toxicological aspects of our 3D graphene nanostructures. Toxicologists have already shown that in several cases, especially after inhalation, nanomaterials induce their toxic effects through an increase in reactive oxygen species (ROS).[40] Elevated ROS levels lead to the activation of antioxidant defense pathways in cells. Once a certain ROS threshold is exceeded, oxidative stress mechanisms are induced. This can lead to severe damage of biomolecules (lipids, nucleic acids, proteins), the induction of inflammatory reactions, and finally cell death (cytotoxicity).[40,41]

According to the ROS paradigm, we assess whether our synthetic 3D graphene nanostructures (both graphene-coated and processed graphene shells) induce ROS overproduction in the human alveolar epithelial cell line A549 using the DCF (2,7-dichlorofluorescein) assay. Furthermore, by using the MTS (3-(4,5-dimethylthiazol-2-yl)-5-(3-carboxymethoxyphenyl)-2-(4-sulfophenyl)-2*H*-tetrazolium)) assay, we investigated if any triggered ROS is sufficient to lead to acute cytotoxic events in these cells. Both assays were performed using the C@MgO, C@TiO_2, and C-shell samples. By analyzing the ROS production in a cell-free but still biological environment in parallel (see Figure S7 in the Supporting Information) we are able to assess any potential nanoparticle intrinsic reactivity that is independent from the reactions caused by 3D graphene nanoparticle−cell interactions. Due to technical issues, neither the cell-based assay nor the cell-free controls can be measured quantitatively. Thus, we are not able to set cell-based values off against values acquired under cell-free conditions. However, qualitative statements on the reactivity of the samples are possible.

Figure 6 shows the ROS measurement performed on A549 cells. The measured fluorescence values are directly proportional to the amount of ROS in the respective samples.

3-Morpholinosydnonimine (Sin-1) is used as an assay intrinsic positive control in parallel to all sample treatments.

All three nanoparticles analyzed induce a certain amount of ROS, with C@MgO being the least potent inducer, the C-shells being the most potent inducer, and the C@TiO_2 particles ranging in between the first two. While the induction is dose-dependent for C@MgO and C@TiO_2, the C-shells show a very high ROS value already at 5 μg/mL, increasing only marginally with 10 μg/mL. With higher C-shell concentrations fluorescence values further decline.

In nanoparticle-related control experiments (see Figure S8 in the Supporting Information) C@MgO as well as C@TiO_2 particles show only marginal intrinsic reactivity, indicating that ROS values seen in Figure 6 are mainly due to cellular reactions. However, the C-shells lead to a considerable, dose-dependent increase in fluorescence values by themselves, *i.e.*, without cellular contribution. This indicates that the cellular reactions seen in Figure 6 are not solely due to cellular reactions but may also result from direct reactions of the sample nanostructures with the dye. Furthermore, we see that increasing amounts of C-shells, and to a much lesser extent also for C@MgO and C@TiO_2 nanoparticles, quench an existing DCF signal, thus explaining the reduction in fluorescence seen in Figure 6 for the C-shells (see Figure S8 in the Supporting Information).

The question of whether the amount of ROS resulting from the treatment with 3D graphene nanostructures is sufficient to cause cytotoxicity was investigated

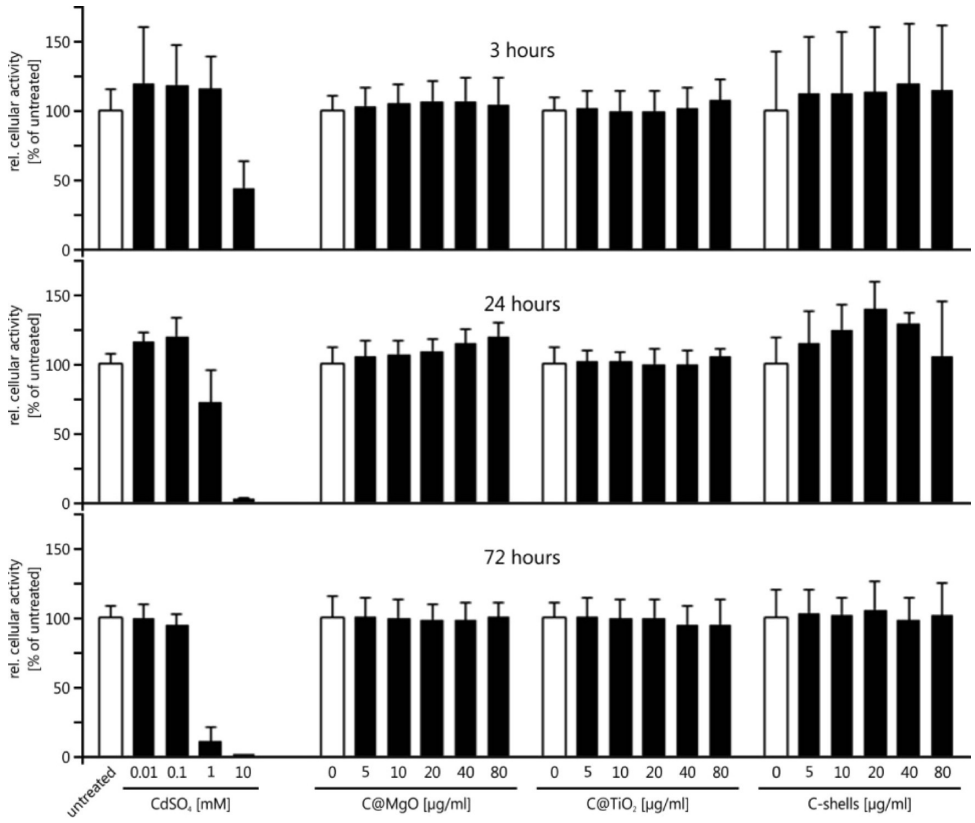

Figure 7. Cell viability is not influenced by any of the nanomaterials tested. A549 cells were treated for 3, 24, and 72 h with the indicated nanomaterial concentrations before the MTS cell viability assay was performed. $CdSO_4$ served as the positive control known to induce cell death in this system. "0 μg/mL" constitutes the solvent controls, which corresponds to 51 ppm Pluronic F-127. Original OD(490) values are blank-corrected and normalized to untreated samples. Data represent the mean of three independent experiments and the standard deviation.

with the MTS assay. In this study, A549 cells were incubated for 3, 24, and 72 h with increasing concentrations of C@MgO, C@TiO_2, and C-shells, respectively. As can be seen in Figure 7 no signs of cytotoxicity, *i.e.*, no reduction in enzymatic activity, was observed for any of the 3D graphene nanostructures for all the time points investigated up to three days.

Nevertheless, the assay internal positive control $CdSO_4$ shows that toxicity can be reliably detected at each time point. Potential interference reactions were again assessed in cell-free control experiments. The measurements indicate **no** significant interference problems for the C@MgO and C@TiO_2 particles. In contrast increasing concentrations of C-shells lead to a marked increase in OD values at 490 nm (without cellular contribution). As no catalytic activity of the particles could be detected, the control wells run with every cell-based experiment (blanks) can be used to correct for this interference (as described in Materials and Methods). Thus, the blank-corrected values given in Figure 7 are comparable between the three nanomaterials as well as the control chemical ($CdSO_4$). It should be noted, however, that despite these initial investigations indicating limited toxicity, whether or not the ROS levels seen here are already above a critical threshold that might lead to long-term or chronic effects is unclear. Damage to lipids, proteins, and nucleic acids as well as inflammatory reactions must also be considered. All of these events could occur without being noticed immediately and might result, for example, locally in some part of the body in adverse health effects. Indeed, greater studies are required to fully comprehend any potential health risks of these and other nanoparticles in general.

The uptake of our 3D graphene nanostructures into A549 cells and their potential impact on cell morphology were analyzed by TEM. To this end, A549 cells were incubated with 40 μg/mL of C@TiO_2 and C-shells for 22 h. Representative micrographs are shown in Figure 8b and c, respectively. In both cases agglomerates appear intracellularly most likely in membrane-enclosed compartments (Figure 8b″ and c′). For morphological comparison untreated cells are shown in Figure 8a. Even though considerable amounts of both 3D graphene nanostructures are internalized, the cells appear remarkably healthy. To further address the issue of cell morphology, we had a look at the actin cytoskeleton of A549 cells. Supplementary Figure S9 shows a comparison of untreated cells and cells that were incubated with 40 μg/mL of C@MgO, C@TiO_2, or C-shells, respectively. Neither conventional DIC imaging nor fluorescence microscopy yields any influence of the three 3D

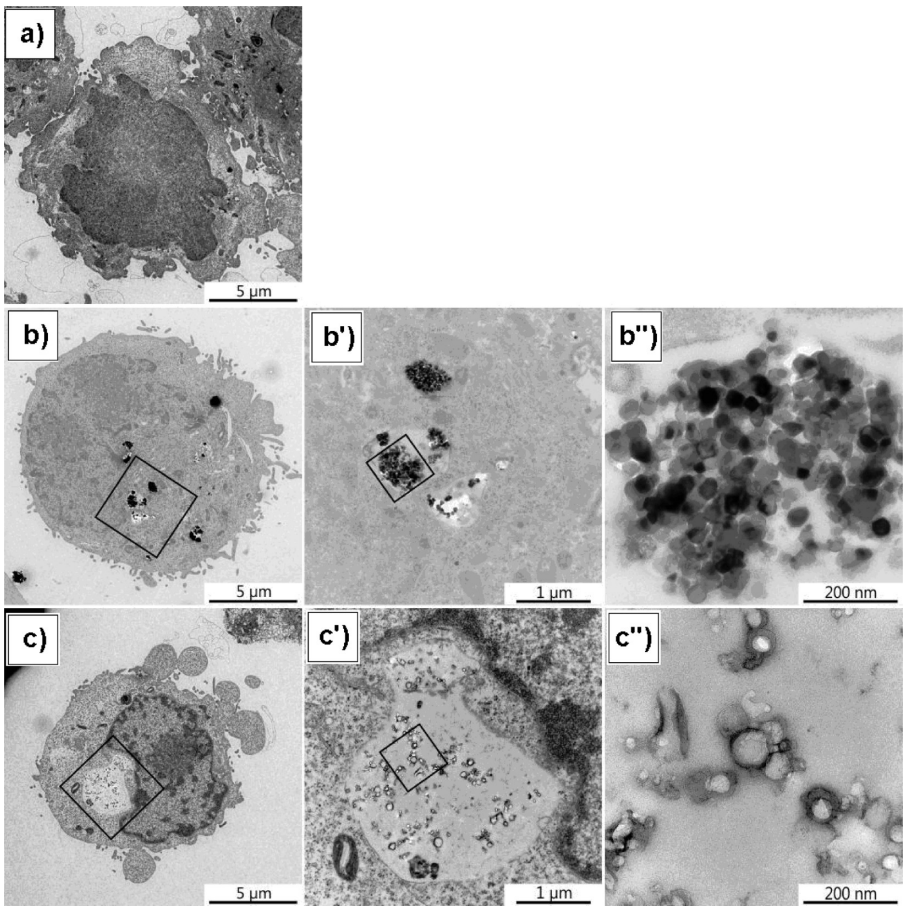

Figure 8. TEM analyses reveal that C@TiO_2 and C-shell particles enter A549 cells without influencing cell morphology. (a) Representative TEM micrograph of an untreated A549 cell. (b–b″) A549 cells treated with 40 μg/mL C@TiO_2 for 22 h. (c–c″) A549 cells treated with 40 μg/mL C-shell particles for 22 h. Increasing magnifications of representative images are shown.

graphene nanostructures tested on cell morphology. These results underscore the cell viability data (MTS) indicating no major impact of the elevated ROS levels on overall cell performance. High-resolution TEM images were also acquired (see Figure S10 in the Supporting Information), and the crystalline structure of the TiO_2 core can even be observed inside the cells. The graphitic nature of the C-shells can also be observed.

CONCLUSIONS

Oxide nanopowders are attractive candidates for encapsulation with few-layer graphene since their manufacture is remarkably facile and inexpensive and can easily be scaled up. Moreover, we demonstrate the ease with which the core can be removed to leave few-layer graphene shells. TEM investigations reveal the few-layer graphene structure is templated by the initial morphology of the oxide nanoparticle, highlighting the potential of the technique for the fabrication of structured 3D graphene nanomaterials. These materials can be further processed to yield hollow structures, and moreover they can be easily functionalized not only through surface attachment of functional groups (*e.g.*, hydroxyl and thiol groups) but also with metal nanoparticle decoration (*e.g.*, Cu). The versatility with which they can be functionalized opens their use in composites, gas sensors, catalysis energy storage, and biomedical application to name a few. Indeed their potential for energy storage applications was also demonstrated. In general, the electrochemical properties imply excellent cyclability and high Coulombic efficiency upon lithium insertion/extraction in addition to an extended plateau region, which suggests that the graphene-coated anatase nanoparticles under study are promising for stable long-life battery applications. Any potential cytotoxicity for such nanomaterials was analyzed using few-layer graphene-coated MgO and TiO_2 and processed C-shells. According to the ROS paradigm,[41] their potential to induce ROS was examined. Even though all three particle types lead (to a certain extent) to elevated ROS levels in our *in vitro* system, no acute toxicity could subsequently be detected, even after three days of incubation. Furthermore, morphology and cytoskeletal architecture remain unperturbed in treated cells. These observations suggest that no acute health risk is to be expected from the handling and usage of such 3D

graphene nanostructures. However, a much more detailed analysis (well beyond the scope of this work) would be required before using these nanostructures in biomedical applications. Overall, our studies suggest 3D graphene nanostructures could be promising alternatives to graphene and carbon nanotubes for a variety of applications, particularly as their production is so facile and cheap.

MATERIALS AND METHODS

A few grams of a selected oxide nanopowder (Al_2O_3, TiO_2, or MgO) serving as the template material was placed in a ceramic crucible, which was then positioned at the center of a horizontal tube furnace. An argon flow (200 mL/min) was established and maintained while the furnace was heated to a temperature of 775 °C. After reaching 775 °C, a second valve was opened to inject an additional flow of argon saturated with ethanol (by bubbling Ar gas (600 mL/min) through liquid ethanol). The reaction was maintained for 1 h, and then the argon/ethanol flow mix was shut off while maintaining a pure Ar (200 mL/min) flow while cooling naturally to room temperature. During this process graphitic layers form over the oxide nanoparticles' surface.[22] After cooling to room temperature the product was removed and subjected to a variety of characterizations. In the case of MgO nanoparticles coated with graphitic layers, some of the material was subjected to treatment in diluted HCl (5 molar) to dissolve away the (core) MgO material so as to leave hollow graphitic shells. After treatment in HCl the material was thoroughly rinsed in deionized H_2O. This process of HCl treatment followed by thorough rinsing was conducted several times, after which the material was dried naturally. In addition, a fraction of the alumina nanoparticles coated with graphitic shells were functionalized to attach −OH groups and subsequently further functionalized to form −SH groups. The hydroxylation was achieved by milling the graphene-coated alumina nanoparticles with KOH using an agate pestle and mortar for 4 h and results in a fine powder. This procedure forms −OH functional groups on the graphitic surface of the nanoparticles through a simple solid-phase mechanochemical reaction at room temperature. After the milling process, the powder was washed several times with deionized water in order to remove the KOH. Finally the powder was filtrated and dried. The functionalization is based on a technique previously demonstrated for carbon nanotubes.[42] Some of the −OH-functionalized graphite-coated alumina nanoparticles were subjected to a second functionalization step to leave thiol (−SH) functional groups on the surface. This was achieved by refluxing the −OH-functionalized graphene-coated alumina nanoparticles in P_4S_{10} and toluene. This process leads to the hydroxide functional groups forming thiol (−SH) groups, as described in ref 43:

$$\mathrm{GCN-OH} + \mathrm{P_4S_{10}} \rightarrow \mathrm{GCN-SH} \qquad (2)$$

where GCN = graphene-coated alumina nanoparticles.

A third and final functionalization step was conducted in which the thiol-functionalized few-layer graphene-coated alumina nanoparticles were subjected to a decoration reaction with Cu using a recently published method.[44] Therefore 1 g of the thiol-capped nanoparticles was dispersed in a solution containing 4 g of $CuSO_4 \cdot 5H_2O$ (~1 g Cu) and 2.98 g of EDTA in 300 mL of deionized water in a glass flask. A 10 mL amount of hydrazine solution (80 wt % in water) was added at room temperature, and the temperature was raised to 90 °C under constant stirring at approximately 1000 rpm. After 20 min reaction time the dispersion was allowed to cool to room temperature, and the copper-decorated particles were separated from the mother liquor by centrifugation and redispersed in ethanol. After a second subsequent washing/centrifugation step with ethanol the particles were dried using a rotary evaporator and stored under an inert atmosphere (argon or nitrogen) to prevent subsequent oxidation of the copper decoration.

Morphology Studies. The morphology of the as-produced nanoparticles coated with few-layer graphene was investigated with high-resolution low-voltage (80 kV) transmission electron microscopy (TEM). The microscope was a JEOL JEM-2010F retrofitted with two CEOS third-order spherical aberration correctors for the objective lens (CETCOR) and the condensor system (CESCOR). Specimen preparation for HRTEM investigations consisted of gently smearing a small quantity of sample between two clean pieces of Al foil. After this a standard Cu TEM grid was gently pressed on some smeared sample. This leads to small fractions of the material adhering to the Cu TEM grid.

Electronic Properties. The electronic properties were investigated using Raman spectroscopy (Thermo-Fisher Smart Raman DXR, excitation laser wavelength = 532 nm), Fourier transform infrared spectroscopy (Bruker 113 Fourier transform spectrometer with a resolution of 0.4 cm^{-1}), and photoemission X-ray spectroscopy (a PHI5600 spectrometer equipped with a monochromatic Al Kα source (1486.6 eV) with an overall spectral resolution of 0.5 eV and operating with a base pressure of 5×10^{-10} mbar).

Cyclic Voltammetry and Specific Capacity Studies. Cyclic voltammetry and charge−discharge cycling were achieved by means of two-electrode Swagelok-type cells using a VMP3 potentiostat (Bio-Logic) loaded into a heating chamber at a temperature of $T = 25$ °C.[45] The working electrodes were placed on an Al-mesh current collector and separated by Whatman borosilicate glass fiber from lithium metal-foil counter-electrodes. For the electrolyte, a 1 M solution of $LiPF_6$ salt in ethylene carbonate/dimethyl carbonate with a volume ratio of 1:1 (Merck) was used. The working electrodes were prepared from a mixture of 80 wt % TiO_2, 10 wt % carbon, and 10 wt % polyvinylidene fluoride binder (Solexis). Note that the graphene layers provide 3.75 wt % carbon as estimated from thermogravimetric measurements (not shown) so that 6.25 wt % Carbon SP (Timcal) was added in order to improve interparticle electronic conductivity. Adding *N*-methyl-2-pyrrolidinone (Sigma-Aldrich) yielded a slurry, which was spread on a circular aluminum grid (*ca.* 10 mm in diameter), dried for 12 h at 100 °C under vacuum, then pressed and dried again for 24 h at 100 °C under vacuum before the Swagelok cells were assembled in an Ar-atmosphere glovebox ($O_2/H_2O < 2$ ppm).

Cytotoxicity Studies. For the nanomaterial suspension for toxicity testing, C@MgO, C@TiO_2, and C-shell nanoparticles were dispersed by sonication (10 min, ultrasonic bath) in 160 ppm Pluronic F-127 (Sigma-Aldrich) to a stock concentration of 250 μg/mL. Nanoparticles were serially prediluted in 160 ppm Pluronic F-127 and finally applied to A549 cells in complete cell culture medium.

Cell Culture. The human alveolar epithelial cell line A549 (ATCC: CCL-185) was grown in complete cell culture medium consisting of RPMI-1640 medium (Sigma-Aldrich) supplemented with 10% FCS (Lonza), 0.2 mg/mL L-glutamine (Gibco), 50 μg/mL penicillin (Gibco), 50 μg/mL streptomycin (Gibco), and 100 μg/mL neomycin (Gibco) at 37 °C and in a 5% CO_2 atmosphere. Cells were subcultured routinely twice a week at approximately 80−90% confluency using 0.5% Trypsin-EDTA (Sigma-Aldrich).

Detection of Reactive Oxygen Species (DCF Assay). The formation of ROS was detected using a 2′,7′-dichlorofluorescein assay. After entry of the cell-permeant H_2DCF-DA (2′,7′-dichlorodihydrofluorescein-diacetate; Molecular Probes, Invitrogen) into cells, intracellular esterases cleave off the diacetate moiety. The resulting H_2DCF is ROS sensitive, and its conversion to the fluorescent form DCF serves as a measure of ROS production. The assay was carried out in 96-well plates (TPP Techno Plastic Products AG). About 2×10^4 A549 cells were seeded in 200 μL of complete cell culture medium per well and grown overnight under standard cell culture conditions. The day after, the medium was replaced by 100 μL of 50 μM H_2DCF-DA in Hank's

buffered salt solution (HBSS) per well, and the cells were incubated for 60 min at 37 °C and 5% CO_2. After two washing steps with prewarmed HBSS 100 μL of the respective NP dilutions in HBSS was applied. 3-Morpholinosydnonimine (Sigma-Aldrich), a nitric oxide donor, was used at a concentration of 100 μM in HBSS and served as the positive control. Fluorescence intensities were measured after 2 h using an FLx800 fluorescence microplate reader (BioTEK Instruments) at an excitation wavelength of 485 nm and an emission wavelength of 528 nm.

Analysis of Cell Viability/Activity (MTS Assay). To assess cell viability/activity, the CellTiter96 AQueous One Solution (Promega) containing MTS as the tetrazolium compound was used according to the manufacturer's protocol. In brief, 8000 A549 cells were seeded in 200 μL of complete cell culture medium per well of a 96-well plate (TPP Techno Plastic Products AG) and grown overnight under standard cell culture conditions. The cells were treated the day after with 200 μL per well of different concentrations of the respective nanoparticles or $CdSO_4$ as the positive control. After appropriate incubation times (3, 24, and 72 h) medium containing stimuli was replaced by 120 μL of MTS working solution (composed of 20 μL of MTS plus 100 μL of phenol-red-free RPMI-1640) per well. The cells were incubated for 60 min at 37 °C and 5% CO_2 before optical density was measured at 490 nm in an EL800 microplate reader (BioTEK Instruments).

Data Processing (MTS and DCF Assay). Blank samples containing no cells but treated exactly the same way (with NP or chemical control stimuli, all washing steps (if necessary), *etc.*) were run with every cell-based assay. Values given in the graphs are blank-corrected and subsequently normalized to the untreated sample. The mean from at least three independent experiments and the corresponding standard deviations are shown.

Transmission Electron Microscopy. For transmission electron microscopy examination, 1×10^6 A549 cells were seeded in complete cell culture medium into T25 cell culture flasks and were grown overnight at 37 °C and 5% CO_2. Respective nanoparticles were applied in 10 mL of complete cell culture medium per T25 flask. After 22 h of incubation the cells were detached from the flask using 0.5% Trypsin-EDTA (Sigma-Aldrich) and pelleted by centrifugation (200*g*, 5 min). The supernatant was discarded, and the cells were resuspended in the remaining drop of medium and sucked up into a capillary tube (Leica-Microsystems). Therein cells were fixed in 3% glutaraldehyde in a 0.1 M sodium cacodylate buffer. After a postfixation step in 2% osmium tetroxide in 0.1 M sodium cacodylate buffer for 30 min the cells were dehydrated through a graded ethanol series followed by acetone and finally embedded in Epon resin (Fluka). Ultrathin sections were contrasted with 2% uranyl acetate and lead citrate[40] before observation in a Zeiss EM 900 (Carl Zeiss MicroImaging) operating at 80 kV and a JEOL 2010F retrofitted with two Cs correctors operating at 80 kV.

Conflict of Interest: The authors declare no competing financial interest.

Acknowledgment. R.G.M. thanks the DFG (RU1540/8-1). C.J. and R.K. acknowledge support by BMBF (grant 03SF0397). A.B., L.F., and M.H.R. acknowledge support from the Sino German Center (project GZ 871). We thank Liliane Diener for exceptionally high-quality TEM analysis of biological samples and Pius Manser for excellent technical support. The work at EMPA was supported by CCMX (MATLIFE) through the project VIGO (contract no. 350601). This work was supported by the Institute for Basic Science (IBS) Korea.

Supporting Information Available: TEM, EDS, cyclic voltammograms, cell analyses, and fluorescent microscopy. This material is available free of charge *via* the Internet at http://pubs.acs.org.

REFERENCES AND NOTES

1. Shevitski B. University of California Los Angeles, CA90095, 2010; 28, reu.physics.ucla.edu/common/papers/2010/shevitski_brian.pdf.
2. Rocha, C. G.; Rümmeli, M. H.; Ibrahim, I.; Sevincli, H.; Börrnert, F.; Kunstmann, J.; Bachmatiuk, A.; Pötschke, M.; Li, W.; Makharza, S. A. M.; *et al*. Tailoring the Physical Properties of Graphene In *Graphene: Synthesis and Applications*; CRC Press, 2011.
3. Zhu, Y.; Murali, S.; Cai, W.; Li, X.; Suk, J. W.; Potts, J. R.; Ruoff, R. S. Graphene and Graphene Oxide: Synthesis, Properties, and Applications. *Adv. Mater.* **2010**, *22*, 3906–3924.
4. Kumar, A.; Reddy, A. L. M.; Mukherjee, A.; Dubey, M.; Zhan, X.; Singh, N.; Ci, L.; Billups, W. E.; Nagurny, J.; Mital, G.; *et al*. Direct Synthesis of Lithium-Intercalated Graphene for Electrochemical Energy Storage Application. *ACS Nano* **2011**, *5*, 4345–4349.
5. Zhang, K.; Fu, Q.; Pan, N.; Yu, X.; Liu, J.; Luo, Y.; Wang, X.; Yang, J.; Hou, J. Direct Writing of Electronic Devices on Graphene Oxide by Catalytic Scanning Probe Lithography. *Nat. Commun.* **2012**, *3*, 1194/1–6.
6. Shen, H.; Zhang, L.; Liu, M.; Zhang, Z. Biomedical Applications of Graphene. *Theranostics* **2012**, *2*, 283–294.
7. Drut, J. E.; Lähde, T. A.; Tölö, E. Graphene: from Materials Science to Particle Physics. *arXiv:1011.0643/1-14*, **2010**
8. Geim, A. K.; Novoselov, K. S. The Rise of Graphene. *Nat. Mater.* **2007**, *6*, 183–191.
9. Park, S.; Ruof, R. S. Chemical Methods for the Production of Graphenes. *Nat. Nanotechnol.* **2009**, *4*, 217–224.
10. Hertel, S.; Waldmann, D.; Jobst, J.; Albert, A.; Albrecht, M.; Reshanov, S.; Schöner, A.; Krieger, M.; Weber, H. B. Tailoring the Graphene/Silicon Carbide Interface for Monolithic Wafer-Scale Electronics. *Nat. Commun.* **2012**, *3*, 957.
11. Li, X.; Magnuson, C. W.; Venugopal, A.; Tromp, R. M.; Hannon, J. B.; Vogel, E. M.; Colombo, L.; Ruoff, R. S. Large-Area Graphene Single Crystals Grown by Low-Pressure Chemical Vapor Deposition of Methane on Copper. *J. Am. Chem. Soc.* **2011**, *133*, 2816–2819.
12. Li, X.; Cai, W.; An, J.; Kim, S.; Nah, J.; Yang, D.; Piner, R.; Velamakanni, A.; Jung, I.; Tutuc, E.; *et al*. Large-Area Synthesis of High-Quality and Uniform Graphene Films on Copper Foils. *Science* **2009**, *324*, 1312–1314.
13. Jacobberger, R. M.; Arnold, M. S. Graphene Growth Dynamics on Epitaxial Copper Thin Films. *Chem. Mater.* **2013**, *25*, 871–877.
14. Schaefer, Z. L.; Gross, M. L.; Hickner, M. A.; Schaak, R. E. Uniform Hollow Carbon Shells: Nanostructured Graphitic Supports for Improved Oxygen-Reduction Catalysis. *Angew. Chem., Int. Ed.* **2010**, *49*, 7045–7048.
15. Yoon, S. M.; Choi, W. M.; Baik, H.; Shin, H. J.; Song, I.; Kwon, M. S.; Bae, J. J.; Kim, H.; Lee, Y. H.; Choi, J. Y. Synthesis of Multilayer Graphene Balls by Carbon Segregation from Nickel Nanoparticles. *ACS Nano* **2012**, *6*, 6803–6811.
16. Chen, Z.; Ren, W.; Gao, L.; Liu, B.; Pei, S.; Cheng, H. M. Three-Dimensional Flexible and Conductive Interconnected Graphene Networks Grown by Chemical Vapour Deposition. *Nat. Mater.* **2011**, *10*, 424–428.
17. Chen, W.; Yan, L. *In Situ* Self-Assembly of Mild Chemical Reduction Graphene for Three-Dimensional Architectures. *Nanoscale* **2011**, *3*, 3132–3137.
18. Bi, H.; Huang, F.; Liang, J.; Tang, Y.; Lü, X.; Xie, X.; Jiang, M. Large-Scale Preparation of Highly Conductive Three Dimensional Graphene and its Applications in CdTe Solar Cells. *J. Mater. Chem.* **2011**, *21*, 17366–17370.
19. Kidambi, P. R.; Bayer, B. C.; Weatherup, R. S.; Ochs, R.; Ducati, C.; Vinga Szabó, D.; Hofmann, S. Hafnia Nanoparticles – A Model System for Graphene Growth on a Dielectric. *Phys. Status Solidi Rapid Res. Lett.* **2011**, *5*, 341–343.
20. Liu, J.; Zhu, Y.; Liang, J.; Qian, Y. Synthesis of In_2O_3/Carbon Core - Shell Nanospheres and their Electrochemical Performance. *Int. J. Electrochem. Sci.* **2012**, *7*, 5574.
21. Rümmeli, M. H.; Kramberger, C.; Grüneis, A.; Ayala, P.; Gemming, T.; Büchner, B.; Pichler, T. On the Graphitization Nature of Oxides for the Formation of Carbon Nanostructures. *Chem. Mater.* **2007**, *19*, 4105–4107.
22. Peng, T.; He, H.; Lv, D.; Pan, M.; Mu, S. Direct Transformation of Amorphous Silicon Carbide into Graphene under Low Temperature and Ambient Pressure. *Sci. Rep.* **2013**, *3*, 1148/1–7.
23. Donaldson, K.; Aitken, R.; Tran, L.; Stone, V.; Duffin, R.; Forrest, G.; Alexander, A. Carbon Nanotubes: A Review of Their Properties in Relation to Pulmonary Toxicology and Workplace Safety. *Toxicol. Sci.* **2006**, *92*, 5–22.

24. Poland, C. A.; Duffin, R.; Kinloch, I.; Maynard, A.; Wallace, W. A. H.; Seaton, A.; Stone, V.; Brown, S.; MacNee, W.; Donaldson, K. Carbon Nanotubes Introduced into the Abdominal Cavity of Mice Show Asbestos-Like Pathogenicity in a Pilot Study. *Nat. Nanotechnol.* **2008**, *3*, 423–428.
25. Feng, L.; Liu, Z. Graphene in Biomedicine: Opportunities and Challenges. *Nanomedicine* **2012**, *6*, 317–324.
26. Star, A.; Joshi, V.; Skarupo, S.; Thomas, D.; Gabriel, J. C. P. Gas Sensor Array Based on Metal-Decorated Carbon Nanotubes. *J. Phys. Chem. B* **2006**, *110*, 21014–21020.
27. Hayden, O.; Nielsch, K. Molecular- and Nano-Tubes. In *Nanotube and Graphene Polymer Composites for Photonics and Optoelectronics*; Springer Science+Business Media, LLC, 2011.
28. Hu, J.; Shi, J.; Li, S.; Qin, Y.; Guo, Z. X.; Song, Y.; Zhu, D. Efficient Method to Functionalize Carbon Nanotubes with Thiol Groups and Fabricate Gold Nanocomposites. *Chem. Phys. Lett.* **2005**, *401*, 352–356.
29. Jiang, C.; Wei, M.; Qi, Z.; Kudo, T.; Honmaa, I.; Zhou, H. J. Particle Size Dependence of the Lithium Storage Capability and High Rate Performance of Nanocrystalline Anatase TiO_2 Electrode. *J. Power Sources* **2007**, *166*, 239–243.
30. Das, S. K.; Bhattacharyya, A. J. High Lithium Storage in Mixed Crystallographic Phase Nanotubes of Titania and Carbon-Titania. *J. Phys. Chem. C* **2009**, *113*, 17367–17371.
31. Zakharova, G.; Jähne, C.; Popa, A.; Täschner, C.; Gemming, T.; Leonhardt, A.; Büchner, B.; Klingeler, R. Anatase Nanotubes as an Electrode Material for Lithium-Ion Batteries. *J. Phys. Chem. C* **2012**, *116*, 8714.
32. Yamaguchi, S.; Asahina, H.; Hirasawa, K. A.; Sato, T.; Mori, S. SEI Film Formation on Graphite Anode Surfaces in Lithium Ion Battery. *Mol. Cryst. Liq. Cryst.* **1998**, *332*, 239–244.
33. Verma, P.; Maire, P.; Novák, P. A Review of the Features and Analyses of the Solid Electrolyte Interphase in Li-Ion Batteries. *Electrochim. Acta* **2010**, *55*, 6332–6341.
34. Dambournet, D.; Belharouak, I.; Amine, K. Tailored Preparation Methods of TiO_2 Anatase, Rutile, Brookite: Mechanism of Formation and Electrochemical Properties. *Chem. Mater.* **2010**, *22*, 1173–1179.
35. Nel, A.; Xia, T.; Mädler, L.; Li, N. Toxic Potential of Materials at the Nanolevel. *Science* **2006**, *311*, 622–627.
36. Reynolds, E. S. The Use of Lead Citrate at High pH as an Electron-Opaque Stain in Electron Microscopy. *J. Cell Biol.* **1963**, *17*, 208–212.
37. Pan, H.; Liu, L.; Guo, Z. X.; Dai, L.; Zhang, F.; Zhu, D.; Czerw, R.; Carroll, D. L. Carbon Nanotubols from Mechanochemical Reaction. *Nano Lett.* **2003**, *3*, 29–32.
38. Cech, J.; Curran, S. A.; Zhang, D.; Aditya Avadhanula, J. L. D.; Kandadai, M.; Roth, S. Functionalization of Multi-Walled Carbon Nanotubes: Direct Proof of Sidewall Thiolation. *Phys. Status Solidi B* **2006**, *243*, 3221–3225.
39. Lohe M. R.; Nickel W.; Grothe J.; Kaskel S. Process for Coating Nanoparticles with Metal by Means of Electroless Deposition Techniques. Patent number WO/2012/072658, June 7, 2012.
40. Larrude, D. G.; Ayala, P.; Maia da Costa, M. E. H.; Freire, F. L., Jr. Multiwalled Carbon Nanotubes Decorated with Cobalt Oxide Nanoparticles. *J. Nanomater.* **2012**, *2012*, 695453/1–5.
41. Popa, A. I.; Vavilova, E.; Täschner, C.; Kataev, V.; Büchner, B.; Klingeler, R. Electrochemical Behavior and Magnetic Properties of Vanadium Oxide Nanotubes. *J. Phys. Chem. C* **2011**, *115*, 5265–5270.
42. Ferrari, A. C. Raman Spectroscopy of Graphene and Graphite: Disorder, Electron–Phonon Coupling, Doping and Nonadiabatic Effects. *Solid State Commun.* **2007**, *143*, 47.
43. Rümmeli, M. H.; Bachmatiuk, A.; Scott, A.; Börrnert, F.; Warner, J. H.; Hoffman, V.; Lin, J. H.; Cuniberti, G.; Büchner, B. Direct Low-Temperature Nanographene CVD Synthesis over a Dielectric Insulator. *ACS Nano* **2010**, *4*, 4206–4210.
44. Acik, M.; Lee, G.; Mattevi, C.; Chhowalla, M.; Cho, K.; Chabal, Y. J. Unusual Infrared-Absorption Mechanism in Thermally Reduced Graphene Oxide. *Nat. Mater.* **2010**, *9*, 840–845.
45. Sun, Z.; Kohama, S.; Zhang, Z.; Lomeda, J. R.; Tour, J. M. Soluble Graphene through Edge-Selective Functionalization. *Nano Res.* **2010**, *3*, 117–125.